CLIMATOLOGY

Antarctic Peninsula warming triggers enhanced basal melt rates throughout West Antarctica

M. Mar Flexas[1]*†, Andrew F. Thompson[1]*†, Michael P. Schodlok[2], Hong Zhang[2], Kevin Speer[3]

The observed acceleration of ice shelf basal melt rates throughout West Antarctica could destabilize continental ice sheets and markedly increase global sea level. Explanations for decadal-scale melt intensification have focused on processes local to shelf seas surrounding the ice shelves. A suite of process-based model experiments, guided by CMIP6 forcing scenarios, show that freshwater forcing from the Antarctic Peninsula, propagated between marginal seas by a coastal boundary current, causes enhanced melting throughout West Antarctica. The freshwater anomaly stratifies the ocean in front of the ice shelves and modifies vertical and lateral heat fluxes, enhancing heat transport into ice shelf cavities and increasing basal melt. Increased glacial runoff at the Antarctic Peninsula, one of the first signatures of a warming climate in Antarctica, emerges as a key trigger for increased ice shelf melt rates in the Amundsen and Bellingshausen Seas.

INTRODUCTION

West Antarctica is undergoing rapid changes associated with both atmospheric and oceanic forcing. The Antarctic Peninsula has experienced sustained warming since at least the 1960s (1, 2), attributed to shifting atmospheric patterns, such as an intensification of the Southern Annular Mode (3). This atmospheric warming, coupled with increases in ocean temperature along the West Antarctic Peninsula (WAP) (4), has led to glacier retreat along the coast (5, 6). State-of-the-art coupled climate models with an active ice sheet project that the supply of freshwater from the continent at the WAP will increase markedly in the coming decades (Fig. 1). Further west, ice shelf volume loss rates have accelerated over the past decades, with changes being particularly pronounced in the Bellingshausen and Amundsen seas (7, 8). The primary factor for ice shelf thickness changes in these regions has been ocean forcing (9), related to an increase in the volume of warm, subsurface Circumpolar Deep Water (CDW) over the continental shelf (10–12).

Ice shelf melt rates throughout West Antarctica vary over decadal (12, 13), interannual (14), and seasonal (15) time scales. Modifications to the surface wind stress over the continental shelf break and their influence over heat transport onto the continental shelf have been cited as a key mechanism to explain variable melt rates at individual ice shelves, particularly in the Amundsen Sea (11, 12, 16). Numerical simulations indicate that the thickness of CDW, particularly in the eastern sector of the Amundsen Sea, responds on short, seasonal time scales to wind fluctuations (17, 18). Over longer time scales, a combination of observations and climate models suggests that greenhouse gas forcing has been responsible for a slow shift in shelf-break winds away from a predominantly easterly orientation to a more westerly orientation over the past century (13). Yet, these longer-term trends represent a small signal compared to much larger interannual and decadal variability, calling into question whether the shelf-break wind mechanism is an effective trigger to explain changes in melt rates across multiple ice shelves and over longer time scales.

Processes occurring near the coast and the ice shelves can also contribute to variations in oceanic heat transport into ice shelf cavities. These processes include the heaving of density surfaces due to the shelf circulation (19), the modification of the ocean stratification due to local freshwater forcing (20), and changes in the vertical structure of boundary currents over the shelf (12, 21). However, only a small number of previous studies have considered nonlocal impacts of forcing perturbations at the Antarctic margins, e.g., (22, 23).

The Antarctic Coastal Current (AACC), a geostrophically balanced oceanic boundary current found along the coast and ice shelf fronts (24), connects the different marginal seas of West Antarctica (25). The AACC originates at the WAP as the result of strong glacial melt concentrating low salinity near the coast (24, 26), although surface wind forcing can also generate sea-surface height (SSH) gradients that support the current (27). Recent observations from instrumented southern elephant seals indicate that the AACC extends from the WAP to the western edge of the Bellingshausen Sea with a likely connection along the Abbot Ice Shelf front into the Amundsen Sea (Fig. 2A). Here, we highlight the impact of the AACC on West Antarctic climate using an ocean numerical model that includes ice shelf cavities and represents key ice shelf–ocean interactions [West Antarctic Ice Shelf model (WAIS) 1080; Fig. 2, B to D; see Methods].

Experimental design

The WAIS 1080 is a high-resolution (horizontal spacing ~3 km) numerical model based on the Massachusetts Institute of Technology general circulation model (MITgcm). It includes a dynamic/thermodynamic sea ice model and reproduces freezing/melting processes in sub–ice shelf cavities via three-equation thermodynamics (see Methods; figs. S1 to S3). The model domain extends from the tip of the Antarctic Peninsula to the western Amundsen Sea (Fig. 2, B to D).

The model represents local sources of freshwater through its sea ice and ice shelf modules. For the ice shelf module, we optimized turbulent exchange coefficients to ensure that the freshwater sources from ice shelf basal melt compared well to the limited available observations; sea ice extent in the model also compares well with observations. A detailed comparison of WAIS 1080 basal melt rates with observations is provided in Methods.

The model's hydrographic state is very close to the observed ocean state. An extensive model/observations comparison is provided in

[1]Environmental Science and Engineering, California Institute of Technology, Pasadena, CA 91125, USA. [2]Jet Propulsion Laboratory, California Institute of Technology, Pasadena, CA 91109, USA. [3]Geophysical Fluid Dynamics Institute and Department of Scientific Computing, Florida State University, Tallahassee, FL 32306, USA.
*Corresponding author. Email: marf@caltech.edu (M.M.F.); andrewt@caltech.edu (A.F.T.)
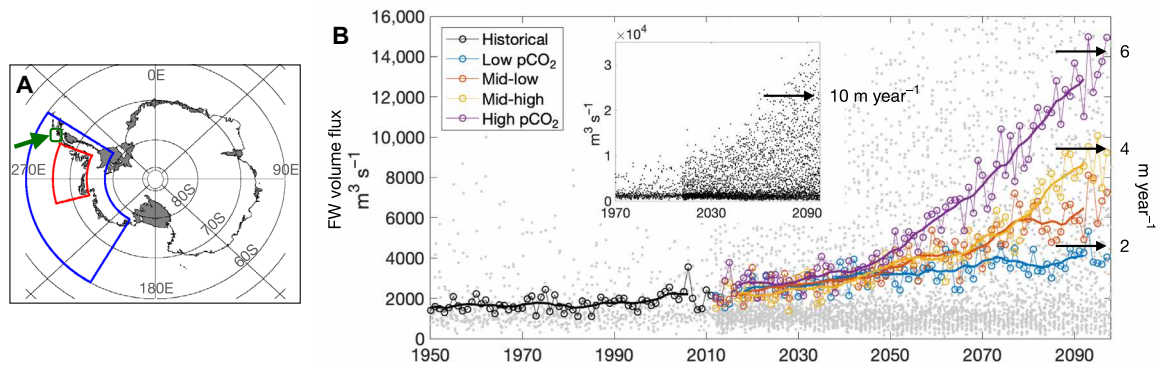†These authors contributed equally to this work.

Fig. 1. Historical and projected continental runoff at the WAP. (**A**) Map of Antarctica highlighting the West Antarctica Ice Shelf (WAIS) model domain (blue box) and the region of freshwater input experiments at the WAP (green box/arrow). The red box shows the domain where the AACC is assessed from elephant seal data (shown in Fig. 2A). (**B**) Historical (1850–2015) and projected (2015–2100) continental runoff at the WAP (shown as freshwater volume flux, in $m^3 s^{-1}$ and in m year^{-1}) from the Community Earth System Model Version 2 model with comprehensive chemistry versions of the atmospheric model (CESM2-WACCM) (*62*), prepared for the Coupled Model Intercomparison Project Phase 6 (CMIP6), representing experiments ranging from low pCO2 to high (SSP1-2.6, SSP2-4.5, SSP3-7.0, and SSP5-8.5) pCO2 emission scenarios (*63*). Gray dots show monthly data from all scenarios. Colors show annual means (circles) and decadal running means (lines) for each scenario. The inset shows the full dataset for all scenarios (monthly data).
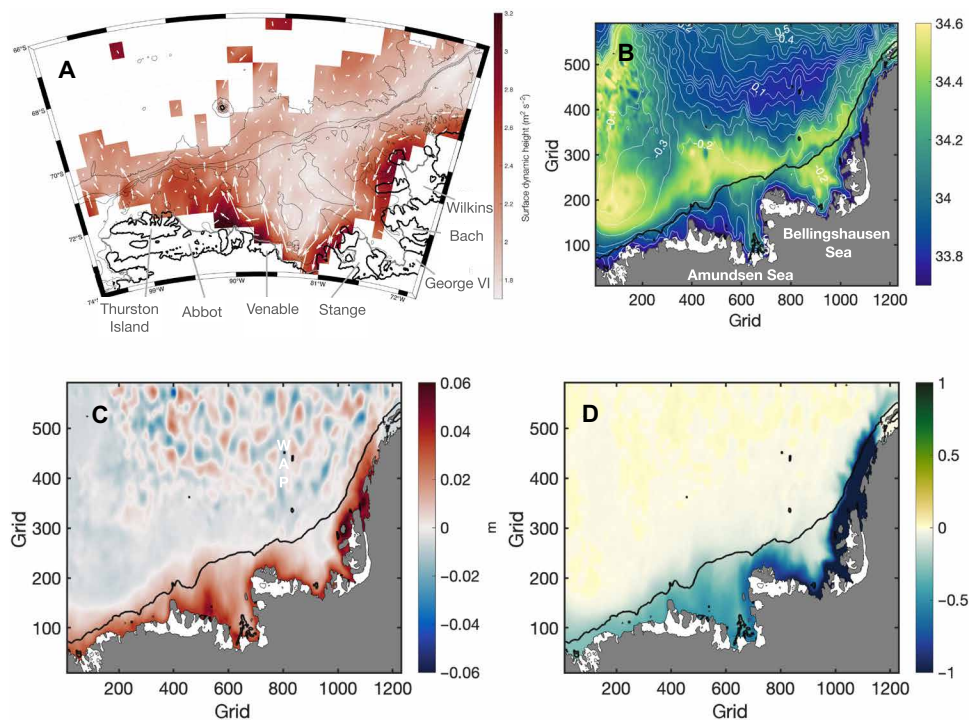

Fig. 2. In situ observations of the AACC and modeled impact of freshwater input at the WAP. (**A**) Surface dynamic height (color), referenced to 400 m, and geostrophic velocity (arrows), based on southern elephant seal data [replotted using the data product from (*25*)]. (**B**) Twenty-seven-year average (1993–2019) modeled salinity at 100 m (color) and SSH (white contours, m) from the control run (no freshwater input at the WAP). (**C**) Difference in SSH from the 10 m year^{-1} run and the control run. (**D**) As in (C), for sea surface salinity.

Methods; we highlight a few key points here. The model successfully reproduces the main water masses (see Methods; figs. S4 and S5), including the near-surface freezing point of Winter Water (WW). While the temperature, salinity, and density values of the deepest waters are well represented in the control run, the model has a fresh bias of about 0.2 practical salinity units (psu) for CDW and WW water masses (figs. S4 and S5). This leads the modeled pycnocline to have a slightly lighter density and to be shallower by about 100 m than observations (fig. S5A). However, this difference does not exert

a large impact on the magnitude of the pycnocline stratification. Differences between observed and modeled modified CDW (0.5°C warmer in the control run) and modeled WW (0.2 psu fresher in the control run) suggest that the model is underrepresenting upper-ocean winter convection and CDW water mass modifications. The continental shelf circulation patterns are reproduced, including warm water intrusions, a recirculation of water masses inside deep troughs of the Bellingshausen and Amundsen seas, and the baroclinic structure of the AACC (see Methods; fig. S6). The reported differences

between observed and modeled hydrography do not affect the main results of this process-based study, which is focused on the influence of stratification changes on WAIS basal melt rates.

Guided by Cook *et al.* (*6*) and climate model projections (Fig. 1), we use the WAIS 1080 configuration to perform a suite of sensitivity studies in which a range of surface continental runoff, ranging from 0 to 10 m year^{-1}, is imposed at the coast along the WAP (see Methods). The range of freshwater perturbations applied in this suite of experiments includes some values that are large compared to predicted perturbations over the coming century (Fig. 1). We include these larger values in this process-based study to assess the robustness of a coastal current freshwater redistribution across a wide range of forcing scenarios.

The model integration period starts in 1992 and runs until 2019. The first year of integration (1992) is considered model spin-up (see details in Methods). In the first 5 years of the control run (1993–1997),

the area-averaged basal melt rates remain stable (black line, Fig. 3A). This 5-year period will be used to assess transient changes following the arrival of the freshwater perturbation. Following 1997, differences in basal melt rates between the control and perturbations experiments are statistically steady. While large increases in basal melt rates occur between 1997 and 2000 and between 2014 and 2017, this variability is present in both control and perturbation experiments and is due to changes in external forcing and boundary conditions (fig. S7). Temporally averaged comparisons between control and perturbation experiments focus on years 2000–2019.

RESULTS

The surface freshwater anomaly is introduced broadly across the WAP. This breadth may represent lateral stirring by ocean eddies, but the results are not qualitatively sensitive to the width of the
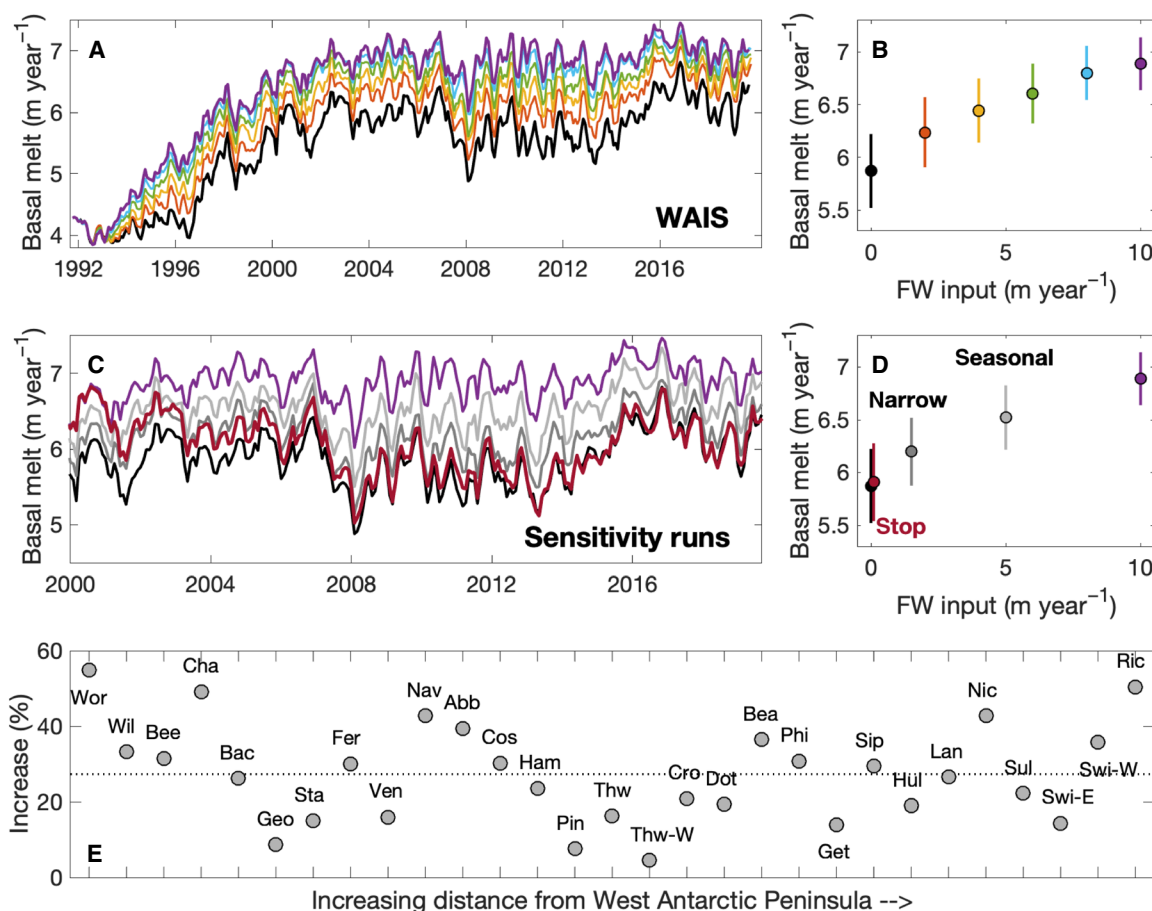

Fig. 3. Impact of freshwater input at the WAP on basal melt rates of the WAIS. (**A** and **B**) Results from sensitivity experiments with WAP freshwater input ranging from 0 to 10 m year^{-1}, shown in colors ranging from black to magenta. (A) Time series of area-averaged basal melt rates for each run over the model integration period (1993–2019) for all ice shelves in the WAIS model domain. (B) Average basal melt (dots) and 1 SD (vertical bars) for each run from 2000 to 2019. (**C** and **D**) Sensitivity of basal melt rates to the freshwater input imposed at the WAP. Using a freshwater input of 10 m year^{-1} at the coast, we test changes in the width and temporal variability of the freshwater forcing at the WAP. In test run "narrow" (in dark gray), the freshwater is imposed over a narrow band of 30 km from the coast. In "seasonal" (light gray), the freshwater input was imposed only from January to May. In "stop" (red), the freshwater input imposed in the 10 m year^{-1} run stops in January 2000. The control run (black) and the 10 m year^{-1} run (magenta) are plotted for reference. For freshwater volume equivalents and details of the freshwater input, see fig. S3. (C) Time series of area-averaged basal melt rates for each sensitivity run for all WAIS ice shelves (years 2000–2019). (D) Average basal melt (dots) and 1 SD (vertical bars) for each sensitivity run from 2000 to 2019. (**E**) Percentage increase in area-averaged basal melt rates for the WAP freshwater input of 10 m year^{-1} compared to the control run (no freshwater input) for each ice shelf from 2000 to 2019. See full ice shelf names in fig. S2. The horizontal dotted line is the average of the percentage change across all ice shelves (roughly 30%).
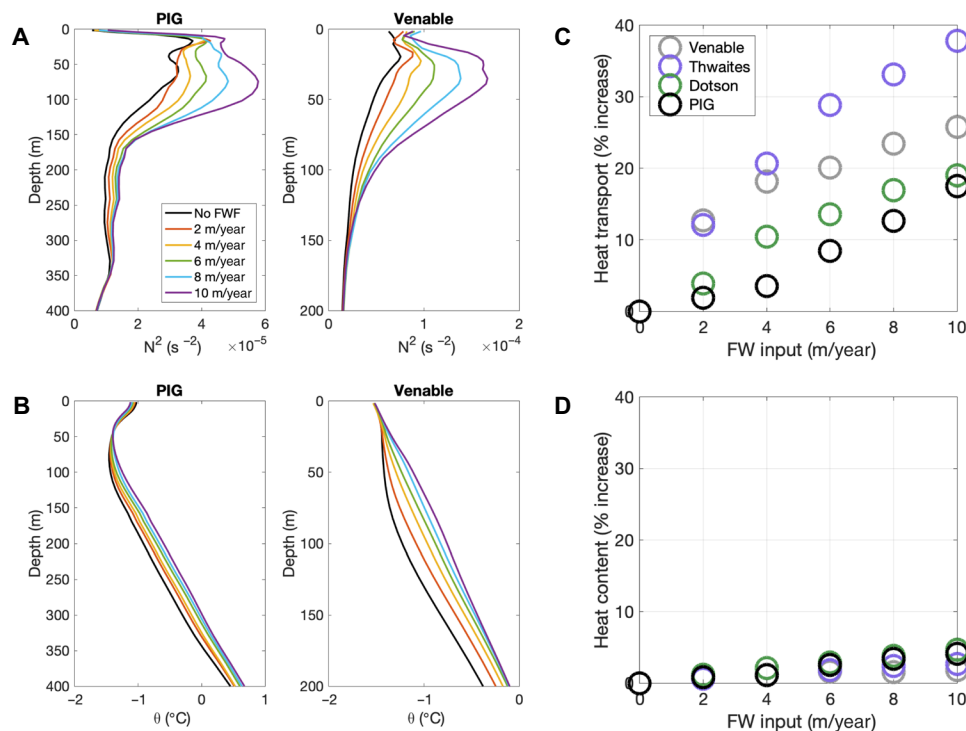
Fig. 4. Mechanism for enhanced basal melt rates throughout West Antarctica. (**A**) Stratification (N^2; Eq. 1) in front of Pine Island Glacier (PIG; Amundsen Sea) and Venable Ice Shelf (Bellingshausen Sea) from experiments with freshwater input ranging from 0 to 10 m year^{-1} (time-averaged over years 1993–1997). (**B**) Same as (A), for potential temperature. (**C**) Changes in net heat transport for PIG [0.9 terawatt (TW) in the control run], Venable (0.5 TW in the control run), Dotson (0.6 TW in the control run), and Thwaites ice shelves, given as percentage increases of each run with respect to the control run. (**D**) Same as (C), for changes in vertically integrated (400 m to bottom) heat content in front of each ice shelf. Heat content in the control run is 0.3 GJ m^{-2} for PIG, 0.4 GJ m^{-2} for Thwaites, 0.5 GJ m^{-2} for Venable, and 0.3 GJ m^{-2} for Dotson.

anomalous forcing (see Methods; Fig. 3, C and D, and fig. S3). The freshwater anomalies are transported away from the WAP within the AACC, and a freshwater anomaly is recorded downstream in the Bellingshausen and Amundsen Seas after a period of 1 and 2 years, respectively (fig. S8). Freshwater anomalies are confined to a narrow region along the coast, except in the central Amundsen Sea, where a broader freshening signal is observed (Fig. 2, B and D). The AACC also strengthens following the perturbation, as evidenced by a positive SSH anomaly near the coast (Fig. 2C).

In addition to a strengthening of the AACC and a modification of surface water properties remote from the forcing location, basal melt rates for all West Antarctic ice shelves increase in response to the WAP perturbation. The impact of the freshwater perturbation is observed in the first 5 years of the model runs (years 1993–1997) as an increasing difference of the WAIS domain-averaged, or area-averaged, melt rates between control and perturbation experiments (Fig. 3A). Following this period, differences in melt rates remain steady.

The WAIS-averaged basal melt rates show a positive, near-linear relationship to the freshwater input (Fig. 3B). At the maximum perturbation (10 m year^{-1}), melt rates increase by roughly 20% (Fig. 3B). Melt rate increase across individual ice shelves can vary substantially, even when ice shelves are in close proximity (Fig. 3E). The area-averaged melt rate increase for individual ice shelves ranges between 5 and 60%, and the average of this percentage change across all ice shelves is roughly 30% (Fig. 3E). These values are insensitive to averaging periods within 2000–2019. Interannual variations, likely

related to atmospheric and oceanic forcing, can still overwhelm this steady perturbation (Fig. 3A).

Changing the width and temporal variability of the freshwater input does not change the main results. To examine the sensitivity of the basal melt rates to the freshwater forcing, we performed three additional sensitivity experiments in which we modified the width and temporal variability of the freshwater input in the 10 m year^{-1} run [see Fig. 3 (C and D) and fig. S3 for details]. In one run [labeled "narrow" in Fig. 3 (C and D)], the freshwater input was forced over a narrow band of 30 km from the coast (as compared to a 300-km offshore extent in the 10 m year^{-1} run). In a second test (labeled "seasonal"), the freshwater input was imposed only from January to May, following the seasonal signal of the AACC at the WAP reported in Moffat et al. (26). Last, we performed a test in which the freshwater input stops in January 2000 [run labeled as "stop" in Fig. 3 (C and D)]. The response of the basal melt rates to these different forcing scenarios remains qualitatively the same. Quantitatively, changes in basal melt rates are directly dependent on the total freshwater flux imposed at the WAP (Fig. 3D and fig. S3). The basal melt rates decrease when the freshwater forcing stops (red line), returning to the unperturbed basal melt rate levels in about 10 years. This highlights the approximately linear relationship between freshwater flux and basal melt rates in this suite of experiments.

Overall, Bellingshausen Sea ice shelves experience a stronger response to the WAP perturbations as compared to ice shelves in the Amundsen Sea (Fig. 3E) due to their proximity to the forcing region. However, the basal melt rate response is not uniform across all ice

shelves, suggesting that local mechanisms are at play, likely related to bathymetric and hydrographic conditions in front of individual ice shelves. To confirm the influence of the freshwater forcing, we consider the vertical stratification and heat transport at several ice shelf fronts (see Methods). In all cases, the downstream propagation of the freshwater anomaly results in an increased vertical stratification near the coast, largely confined to the upper 200 m (Fig. 4A). This enhanced stratification leads to a warming of the ocean below 200 m (Fig. 4B). However, there is a larger relative increase in heat transport into the cavity at the ice shelf front (Fig. 4C) as compared to the relative increase in heat content in the CDW layer (Fig. 4D). The heat transport into the cavity increases roughly at the same rate as the basal melt rates. As warmer water flows into the ice shelf cavity, enhanced melt rates will lead to a stronger outflow of glacially modified CDW [28]. If this water is then entrained into the near-surface circulation, it would increase the density anomaly and volume flux of the AACC, providing a potential positive feedback to the strength of this current.

DISCUSSION

To investigate the mechanisms behind the increase in heat transport into the cavity and ice shelf melt rates, we considered how velocity and temperature fields, as well as heat transport, diagnosed for vertical sections located at the termini of major WAIS ice shelves (see locations in figs. S1 and S2), were modified in the perturbed simulations as compared to the control run. Here, we describe these changes for a section in front of Pine Island Glacier (PIG) between the control run and the 10 m year^{-1} perturbation run (Fig. 5); this

section is similar to other ice shelves (see fig. S9 for anomalies at Thwaites Ice Shelf). In both simulations, the velocity field is dominated by a cyclonic circulation that carries water into the ice shelf cavity on the eastern side and flows out of the cavity on the western side of the section (Fig. 5A), consistent with observations [29]. In the perturbation runs, this cyclonic circulation is intensified. There is a stronger velocity change in the upper 300 m, which is linked to the strengthening of the AACC, but the intensified inflow and outflow extend throughout the water column (Fig. 5B). The temperature field (Fig. 5C) has a two-layer structure with relatively cold Antarctic surface water lying over the modified CDW; these two water masses are roughly separated by the 0°C isotherm. As the AACC strengthens, the entire water column warms, except for a thin ~50-m layer near the surface (Fig. 5D). However, the warming is strongest in the pycnocline at a depth between 300 and 400 m, where the temperature change can exceed 0.5°C. Furthermore, this change is confined to the coastal region (Fig. 5D). Last, the heat transport (Fig. 5, E and F) shows an intensification of both positive and negative heat fluxes associated with water flowing in and out of the cavity, respectively, although the net heat transport into the cavity increases (Fig. 4C). While the heat flux increases broadly across the ice shelf front due to additional heat trapped at depth, the heat flux has its largest increase on the eastern side of the section at a depth of roughly 400 m, corresponding to the peak temperature increase at the base of the pycnocline.

To further assess the degree to which modification to the AACC traps heat at depth, we carried out a heat budget analysis for a region bounded by PIG to the south and the entrance of the Amundsen
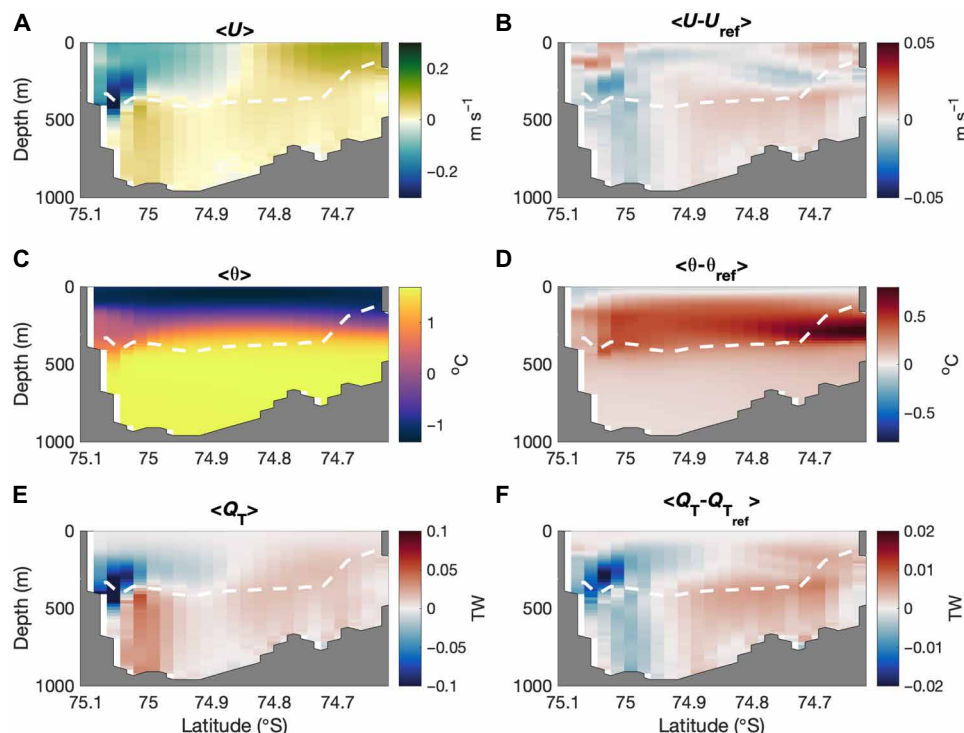

Fig. 5. Hydrography and lateral heat transport near Pine Island Glacier. Meridional section in front of Pine Island Glacier (location shown in fig. S1) showing (**A**) velocity (m s^{-1}; positive eastwards), (**C**) potential temperature (°C), and (**E**) heat transport, Q_T (TW; positive into the cavity) from the 10 m year^{-1} run. (**B**, **D**, and **F**) Same as (A), (C), and (E), for the difference between the 10 m year^{-1} run and the control run. The symbol < > indicates time-averaged fields over years 2000–2019; "ref" indicates fields from the control run (without FW input). Ice draft along the ice shelf front is shown as a dashed white line.

Sea Embayment (ASE) to the north (Fig. 6; see section location in fig. S1). Specifically, we compared the relative importance of changes in horizontal and vertical heat fluxes to attribute the increased heat transport in front of the ice shelf cavities in the perturbation runs. Changes in temperature and velocity begin to occur roughly 2 years after the freshwater flux is imposed at the WAP (Fig. 6). When freshwater is imposed at the WAP, the AACC shoals and increases in strength, due to increasing stratification.

The largest increase in horizontal heat transport is localized to the coast, although an analysis of zonal sections, moving progressively from the shelf break to the coast, does reveal some changes in heat transport close to the shelf break (e.g., fig. S10). For example, because of the proximity of the AACC to the shelf break at the easternmost Amundsen Sea (near Abbot Ice Shelf), imposed freshwater anomalies may modify the stratification, geostrophic circulation, and heat transport at the easternmost side of the Amundsen Sea. At this location, the combined effect of changes in the AACC and at the shelf break may contribute to the increased heat transport toward the coast, ultimately reaching ice shelf cavities in the Amundsen Sea. In contrast, the zonal sections do not show the heat being transferred from the shelf break to the coast along the major troughs in the central Amundsen Sea. Changes in the heat transport within the trough at the ASE section (Fig. 6) are much smaller than those occurring along the coast. In addition, changes in heat transport along these zonal sections are correlated with the structure of the AACC (surface intensified), not the deeper trough circulation. Therefore, we conclude that changes in heat transport at the shelf break do not

have a strong influence on basal melt rate variability in these perturbation experiments.

A comparison of temperature differences between the 10 m year^{-1} and the control run in the ASE and PIG sections shows that the observed changes in temperature are localized near the ice shelves (Figs. 5D and 6D). We propose that these temperature changes are linked to a suppression of vertical mixing, which reduces both the turbulent transport of colder surface water to depth and the ventilation of heat from the CDW layer to the ocean surface and ultimately the atmosphere. The increase in vertical stratification that accompanies the freshwater perturbation and is propagated throughout the West Antarctic shelf seas reduces the vertical heat flux within the pycnocline (Fig. 7, B and D). The reduction in vertical mixing leads to a convergence of heat in the CDW layer and a larger reservoir of heat available to be transported into the ice shelf cavity. Again, the focusing of these temperature changes near the coast implicates the strengthening of the AACC as the primary mechanism, as opposed to processes happening more broadly over the continental shelf or at the shelf break. Last, modifications to the AACC may also give rise to stratification changes that increase the baroclinic circulation in the ice shelf cavity following thermal wind balance and are more effective at carrying these warmer waters into the cavity.

Increased heat transport into the ice shelf cavity may arise from either a change in the partitioning of vertical and lateral heat fluxes, a change in the relative importance of barotropic and baroclinic circulations (21), or some combination of the two. Heat budgets over the continental shelf along the WAP suggest that heat flowing onto
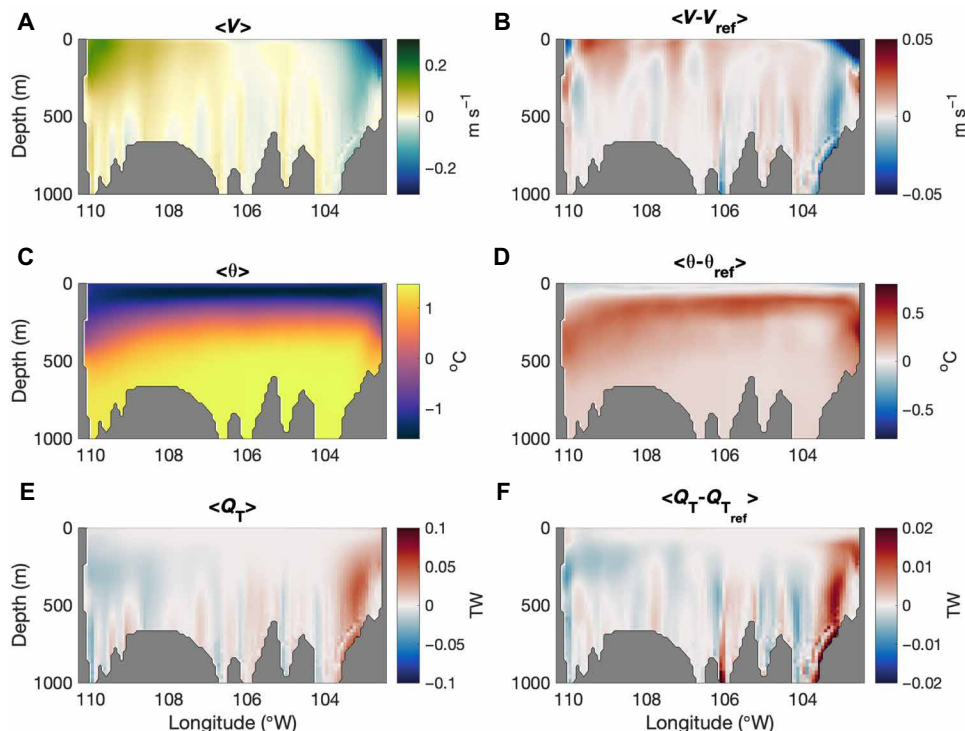

Fig. 6. Hydrography and lateral heat transport at Amundsen Sea Embayment. Zonal section in the Amundsen Sea Embayment (location shown in fig. S1) showing (**A**) velocity (m s^{-1}; positive northward), (**C**) potential temperature (°C), and (**E**) heat transport, Q_T (TW; positive southward, toward the ice shelves) from the 10 m year^{-1} run (left panels). (**B**, **D**, and **F**) Same as (A), (C), and (E), for the difference between the 10 m year^{-1} run and the control run. The symbol < > indicates time-averaged fields over years 1993–1997; "ref" indicates fields from the control run (without FW input).

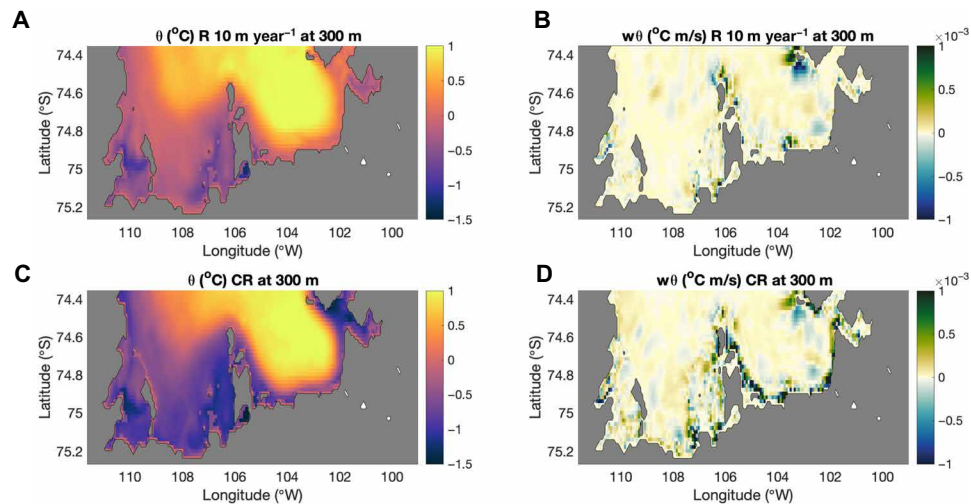**Fig. 7. Hydrography and vertical heat transport near at Amundsen Sea Embayment.** (**A**) Potential temperature (°C) and (**B**) vertical heat flux, $w\theta$ (°C m s^{-1}) at 300 m inside the Amundsen Sea Embayment from the 10 m year^{-1} run in November 1995. (**C** and **D**) Same as (A) and (B) for the control run (CR). This level was representative to describe the vertical heat transport within the pycnocline.
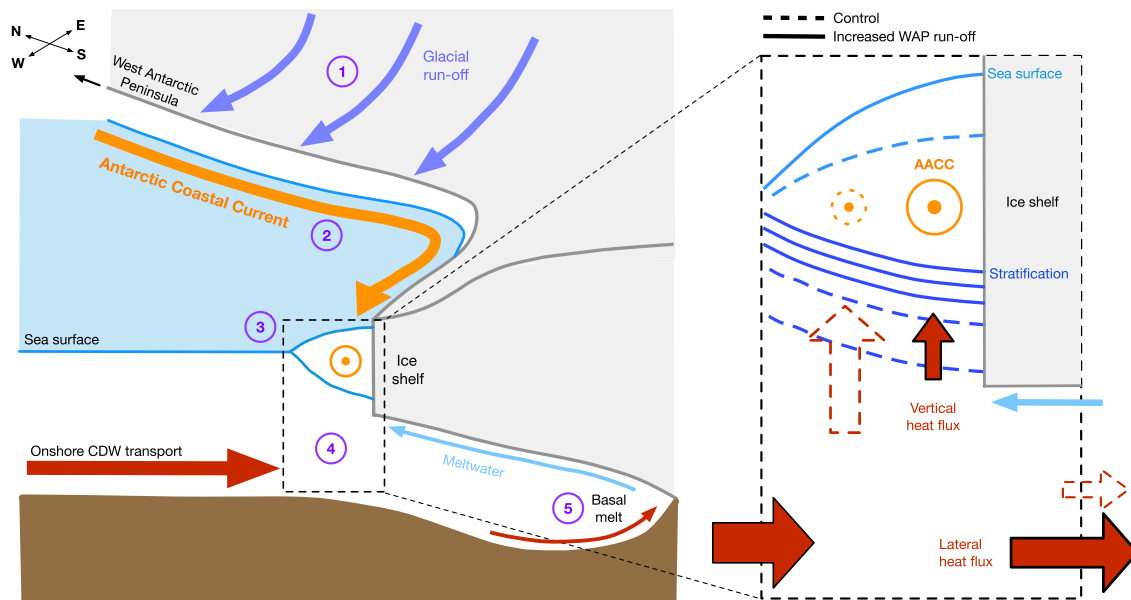

Fig. 8. Summary of mechanisms by which Antarctic Peninsula warming increases basal melt rates of WAIS. (1) Multidecadal-scale warming trends over the Antarctic Peninsula have led to increased glacial runoff and freshening along the coast. (2) The influx of freshwater strengthens the westward-flowing, geostrophically balanced AACC, which (3) modifies the sea surface height and stratification in front of floating ice shelves. (4) The enhanced stratification traps more heat at depth and a larger proportion of warm water is directed into ice shelf cavities, (5) leading to enhanced basal melt rates.

the continental shelf is balanced by a combination of (i) vertical mixing and heat loss to the atmosphere and (ii) lateral transport and heat loss to marine-terminating glaciers (*20*, *30*). An important aspect of our proposed mechanism is that the AACC forms at scales O (10 km) that are not resolved by climate simulations. Thus, the enhancement in basal melt rate that we find in our experiments would represent a missing source of freshwater to the upper ocean. Here, we focus on how the AACC influences basal melt rates, but there may be additional implications, related to the change in stratification, such as an expansion of sea ice extent (*31*–*33*).

In summary, the delivery of freshwater to the West Antarctic shelf seas via the AACC (Fig. 2) increases vertical stratification in front of all WAIS ice shelves (Fig. 4A), which traps heat at depth (Fig. 4B), increases the transport of heat into the ice shelf cavity (Fig. 4C), and enhances basal melt rates (Fig. 3). These results suggest an expansive role for the AACC in West Antarctica. A schematic summarizing the physical processes that give rise to increased basal melt rates following a coastal freshwater perturbation is shown in Fig. 8. As marginal seas are salinity-stratified, export of freshwater from the WAP has a substantial impact on stratification near the coast. If the stratification

is sufficiently strong, it can suppress vertical mixing arising either from wind forcing or brine rejection during sea ice formation [e.g., (*34*)]. This, in turn, suppresses vertical heat transport, such that less of the CDW heat content is mixed toward the surface and lost to the atmosphere (*30*, *35*). Instead, heat is preferentially diverted into the ice shelf cavity. Our simulations support growing observational evidence that the AACC transports freshwater anomalies and modifies stratification broadly throughout West Antarctica (*25*, *26*).

The rate of basal melt in West Antarctica is sensitive to a range of atmospheric, oceanic, and glacial processes with various characteristic time scales. Here, we show that changes in the strength and stratification of the AACC, occurring near the coast, modify heat transport into ice shelf cavities all along the path of the AACC. Previous studies have largely focused on shelf-break controls on cross-shelf, or along-trough, heat transport, with an emphasis on interannual time scales (*11*, *12*). Over the satellite altimetry record, dating back to the early 1990s, the ice shelves of Antarctica have been melting faster than steady state (i.e., losing mass), suggesting that decadal-scale or longer-term changes are active. Changes occurring in the Amundsen Sea have been implicated in bottom water formation rates in the Ross Sea (*36*). Our results extend this inter-sea relationship dynamically to ice shelf melt rates, spatially to a much larger extent of West Antarctica (eastward to the WAP), and temporally to the almost centennial-scale record of warming at the Antarctic Peninsula. Longer-term (e.g., decadal-scale and longer) feedbacks between shelf overturning circulation, inter-sea exchange, and ice shelf basal melt remains a critical area to explore and may be required to improve future sea level rise projections.

METHODS

Numerical model configuration

The WAIS 1080 model is based on the MITgcm, which includes a dynamic/thermodynamic sea ice model (*37*). Freezing/melting processes in the sub–ice shelf cavity are represented by the three-equation thermodynamics of Hellmer and Olbers (*38*) with modifications by Jenkins *et al.* (*39*) as implemented in MITgcm by Losch (*40*). Exchanges of heat and freshwater at the base of the ice shelf are parameterized as diffusive fluxes of temperature and salinity using the transfer coefficients of Holland and Jenkins (*41*) that are functions of the friction velocity. This system of equations is solved to determine the height change of the ice shelf draft, which is converted into a virtual freshwater flux, basal melt. The freshening of the water column through melting, or alternatively the increase in salinity due to freezing, is proportional to the salinity at the base of the ice shelf.

The model domain is derived from the global Latitude-Longitude-Polar Cap configuration (LLC) used by the Estimating the Circulation and Climate of the Ocean (ECCO-MITgcm) project (*42*) with a nominal horizontal grid spacing of ~3 km (LLC 1080) on the Antarctic continental shelf and comprises the region used in Schodlok *et al.* (*15*). Our model configuration choices include a flux-limited, seventh-order, monotonicity-preserving advection scheme (*43*) and the modified Leith scheme of Fox-Kemper and Menemenlis (*44*) for horizontal viscosity. Vertical viscosity and diffusivity are parameterized according to the K-profile parameterization (*45*). Bottom drag is quadratic (drag coefficient, $C_D = 2.1 \times 10^{-3}$), and side drag is free slip. The vertical discretization uses 113 vertical levels of varying thickness to capture the deep part of the cavities near the grounding line. Partial cells (*46*) are used to represent the sloping sea floor. The bathymetry is a blend of the International Bathymetric Chart of the Southern

Ocean (*47*) and Bedmachine Antarctica (*48*) (fig. S1). Ice shelf draft is derived from Bedmachine Antarctica. Turbulent exchange coefficients for heat and salt at the ice-ocean interface were optimized for year 1992 using initial guess values from Nakayama *et al.* (*49*) where applicable; otherwise, the coefficients were set to default values of 10^{-4} [e.g., (*15*)]. Transfer coefficients were optimized using basal-melt reference values from Rignot *et al.* (*50*) where available. Surface forcing is taken from European Centre for Medium-Range Weather Forecasts (ECMWF) reanalysis version 5 (ERA5) (*51*). Initial conditions and boundary conditions for hydrography and sea ice are derived from a coarse resolution global state estimate (~18-km horizontal grid spacing, LLC 270) for the integration period 1992 to 2019. This ocean state estimate does not include ice shelf–ocean interactions.

Because of the difference in grid spacing between the global state estimate (LLC 270, ~18 km) and our model (WAIS 1080, ~3 km), we let the WAIS 1080 model adjust geostrophically by integrating it without external forcing and with a small time step. This leads to the initialization of the WAIS 1080 model from the state estimate to be very close to a realistic ocean state. After initialization, we apply external forcing; the hydrography in the ice shelf cavities adjusts within half a year of integration. We consider the first year of integration (1992) as model spin up, and the model analysis is performed for years 1993 to 2019.

Preliminary runs showed a sensitivity to the initialization of the AACC in the WAP. Because of the coarse grid spacing of the LLC 270 simulation, the boundary conditions do not resolve the structure of the AACC. Thus, we introduce a baroclinic coastal current at the eastern boundary of the model domain over five grid points and balance the extra inflow to conserve volume. These boundary conditions were guided by comparison of the model's representation of the AACC in the WAP and existing observations (*26*).

Basal melt rates are two-dimensional variables given for each grid of the model domain at the ice shelf-ocean interface. Basal melt rates in Fig. 3 are area averages over the entire ice shelf. Values for the ocean's vertical stratification and lateral heat transport, shown in Fig. 4, are calculated across vertical sections obtained in front of the main ice shelves. The sections considered in this study are indicated in fig. S1.

Stratification is estimated using the CSIRO-script *sw_bfrq*, which calculates the local buoyancy frequency squared (N^2) (i.e., the Brunt-Väisälä frequency squared) at the mid-depths from the equation

$$N^2 = -g\rho^{-1} \partial\rho/\partial z \tag{1}$$

where $g = 9.8$ m s^{-2} is the gravitational acceleration and ρ is the local potential density. The meridional heat transport across a zonal section is calculated as

$$Q_T = C_p \int_{z=-h}^{z=0} \int_{x_1}^{x_2} \rho(x,z)\, v(x,z)\, [\theta(x,z) - \theta_f]\, dx\, dz \tag{2}$$

where v is the meridional velocity, θ is potential temperature, $C_p = 4000$ J kg^{-1}°C^{-1} is the specific heat capacity of seawater, and $\theta_f = -1.85$°C is the freezing point temperature of water at the ocean surface. The ocean heat content, H, is calculated (integrating from 400 m to the bottom) as

$$H = C_p \int_{z=-h}^{z=-400m} \rho(z)\, [\theta(z) - \theta_f]\, dz \tag{3}$$

We use the continental runoff distribution in the LLC 270 model configuration to perform a number of sensitivity experiments on surface freshwater input at the WAP. In LLC 270, the freshwater discharge at the WAP is introduced as a surface freshwater input (θ = 0°C; S = 0 psu) with maximum values near the coast decreasing exponentially to zero at a distance of 300 km offshore (fig. S3). For the control run, we set the LLC 270 continental runoff to zero over the entire WAIS 1080 domain. For the main suite of experiments analyzed in this contribution, we impose a constant surface freshwater input at the WAP, ranging from 0 to 10 m year^{-1} at the coast. For reference purposes, for each experiment, we give the freshwater volume flux imposed at the WAP as (i) volume flux per kilometer of coastline, (ii) volume flux in m^3 s^{-1}, and (iii) glacier ice discharge equivalent calculated using an ice density of 917 kg m^{-3} (52). The results are not qualitatively sensitive to the width of the anomalous forcing but rather to the total freshwater volume imposed at the WAP.

Model evaluation

The model represents local sources of freshwater through its sea ice and ice shelf modules, whose parameters are chosen to be as close to observations as possible. To evaluate the model representation of sea ice cover and extent, we have compared the model output to SSM/I (special sensor microwave/imager) monthly observations (available at https://earth.gsfc.nasa.gov/cryo/data/arcticantarctic-sea-ice-time-series). The sea ice extent in the model compares well with observations. In the model, sea ice area is about 25% larger for the maxima and about 16% lower for minima than observations. The correlation coefficient of the maxima is 0.89 for sea ice area and 0.86 for sea ice extent, whereas the correlation coefficient for minima is only 0.58 for area and 0.57 for extent. The differences in sea ice freeze and melt are caused, in part, by the zero-layer thermodynamic sea ice model, which does not account for sensible heat storage in the ice [cf. Losch et al. (37), their figure 7].

For the ice shelf module, we optimized turbulent exchange coefficients using initial guess values from Nakayama et al. (49), which were derived on the same LLC 1080 grid (with fewer ice shelves). This assures that the freshwater sources from ice shelf basal melt are well represented compared to the limited observations. The WAIS 1080 basal melt rates compare well to observations (see table S1) (50) within 1 standard deviation (SD). The only exception is Wordie Ice Shelf, a very small ice shelf, for which the mean model melt rate is only 10% of observations.

For model evaluation purposes, we use hydrographic data from the Marine Mammals Exploring the Oceans Pole to Pole (MEOP-CTD) database (53) (www.meop.net/), collected by southern elephant seals (Mirounga leonina) and crabeater seals (Lobodon carcinophaga) instrumented with CTD-SRDLs. Temperature and salinity data, calibrated using historical data (54, 55), have estimated uncertainties of ±0.02°C for temperature and ±0.02 psu for salinity. Details on temporal and spatial coverage in the Bellingshausen Sea can be found in Zhang et al. (55) and Schubert et al. (25).

To compare hydrographic properties from the MEOP database and our model output, we generated a histogram in θ-S space of all available seal data and 1 year (1998) of temperature and salinity fields from the control run in the Bellingshausen Sea (south of 72°S, and between 72°W to 90°W) (fig. S4). The model reproduces the main water masses, including the near-surface freezing point of WW, although the model shows a fresh bias of 0.2 psu. This bias is clear when comparing the observed versus modeled maximum salinity

values of CDW. In general, the model shows more CDW intrusions and more modified CDW on the shelf than the seal data. Antarctic surface water in the model has more variability than in the seal-based observations. Surface waters in the model are 0.5° to 2°C warmer than those recorded from seal data. Differences in surface water properties between model and seal data can be due to both the seal sampling distribution and errors in seal data accuracy, which are particularly large in the upper 60 m of the water column (53). Part of the difference in hydrographic properties may also be attributed to the discrete nature of seal data versus continuous model averages over ~3-km grid sizes.

In addition, we perform a comparison of conductivity-temperature-depth (CTD) profiles and model output in the Bellingshausen Sea from a hydrographic cruise (56) performed in January 2019 (fig. S5). The model successfully reproduces the main water masses (fig. S5). The deepest waters (0°C, 34.7 psu) are well represented in the model. CDW in the model is about 0.1°C warmer and 0.2 psu fresher than observations. Modified CDW in the model is 0.5°C warmer than observations; this suggests that the model somewhat underrepresents actual CDW watermass modifications. WW is about 0.2 psu fresher in the model consistent with underrepresented upper-ocean winter convection. The modeled pycnocline is offset to lighter density values, hence shallower by about 100 m than in observations (fig. S5A). As CDW and WW are both ~0.2 psu fresher, the pycnocline offset toward lighter density values does not cause a large impact on the stratification of the pycnocline. Near-surface waters in the model (above 10 m) are 0.5° to 2°C warmer and 0.5 psu fresher than observations; this is an improvement from the model-observation comparison performed with seal data (fig. S4). Last, the model successfully reproduces main shelf/slope circulation patterns, such as the strength and structure of the AACC (see below) and CDW intrusions in the Amundsen and Bellingshausen Seas as shown in observations (56, 57).

The AACC in the WAIS 1080 model

Because of the challenges of obtaining observations in coastal regions, the AACC has been best characterized along the WAP, where this current originates and flows south toward the Bellingshausen Sea (26, 58). Recent observations indicate that the AACC extends to the western edge of the Bellingshausen Sea with a likely connection along Abbot Ice Shelf front into the Amundsen Sea (Fig. 2A). The AACC has been modeled and observed in the Amundsen Sea (59, 60), making it a coherent feature throughout West Antarctica. Modeling efforts have shown the circumpolar character of coastal boundary currents and their importance to interbasin exchanges (23, 61). However, the structure of the AACC, and its associated transport, has not been previously assessed in a model of the WAIS 1080 resolution.

The WAIS 1080 model configuration successfully represents the AACC. Figure 2B shows the 27-year averaged (from 1993 to 2019) salinity field at 100 m and the mean SSH field from the same period corresponding to the control run (without freshwater input). The structure of the AACC in the WAIS 1080 model (before any perturbations) consists of a narrow, coastal band of low salinity and relatively high sea surface height (Fig. 2B). This low salinity generates a westward geostrophic current (the AACC) that spans 20 to 50 km off the coast and 100 to 250 m in the vertical, as observed in vertical sections obtained along 87°W (top panels in fig. S6). The structure of the AACC in the WAIS 1080 model is in good agreement with observations of this coastal boundary current at the WAP (26) and at the Bellingshausen Sea (25).

The structure of the AACC changes when freshwater is imposed at the WAP. The freshwater flows south within the AACC and a

freshwater anomaly is found downstream in the Bellingshausen and Amundsen Seas after a period of 1 and 2 years, respectively (fig. S8). The freshwater anomalies freshen the salinity field near the coast and induce a stronger current flowing from the WAP to the Bellingshausen and Amundsen Seas (middle panels in fig. S6).

To understand the sensitivity of the AACC to the freshwater forcing, we perform sensitivity experiments in which we reduce the offshore extension of the freshwater input. In the main suite of experiments, the freshwater anomalies extend 300 km from the coast (middle panels in fig. S6). In the run labeled "narrow" (bottom panels in fig. S6), the freshwater input is forced over a narrow band of 30 km from the coast (see fig. S3 for details). Changing the offshore extent of the freshwater forcing does not qualitatively change the results: The freshwater input at the WAP produces a freshening that leads to a strengthening of the coastal current. Changes in the strength of the AACC are related to the total freshwater imposed at the WAP but not related to the maximum value of freshwater imposed at the coast.

SUPPLEMENTARY MATERIALS

Supplementary material for this article is available at https://science.org/doi/10.1126/sciadv.abj9134

REFERENCES AND NOTES

1. D. G. Vaughan, G. J. Marshall, W. M. Connolley, C. Parkinson, R. Mulvaney, D. A. Hodgson, J. C. King, C. J. Pudsey, J. Turner, Recent rapid regional climate warming on the Antarctic Peninsula. *Clim. Change* **60**, 243–274 (2003).
2. J. F. Carrasco, D. Bozkurt, R. R. Cordero, A review of the observed air temperature in the Antarctic Peninsula: Did the warming trend come back after the early 21st hiatus? *Polar Sci.* **28**, 100653 (2021).
3. G. J. Marshall, A. Orr, N. P. M. van Lipzig, J. C. King, The impact of a changing Southern Hemisphere Annular mode on Antarctic Peninsula summer temperatures. *J. Climate* **19**, 5388–5404 (2006).
4. S. Schmidtko, K. J. Heywood, A. F. Thompson, S. Aoki, Multidecadal warming of Antarctic waters. *Science* **346**, 1227–1231 (2014).
5. A. J. Cook, A. J. Fox, D. G. Vaughan, J. G. Ferrigno, Retreating glacier fronts on the Antarctic Peninsula over the past half-century. *Science* **308**, 541–544 (2005).
6. A. J. Cook, P. R. Holland, M. P. Meredith, T. Murray, A. Luckman, D. G. Vaughan, Ocean forcing of glacier retreat in the western Antarctic Peninsula. *Science* **353**, 283–286 (2016).
7. F. S. Paolo, H. A. Fricker, L. Padman, Volume loss from Antarctic ice shelves is accelerating. *Science* **348**, 327–331 (2015).
8. S. Adusumilli, H. A. Fricker, B. Medley, L. Padman, M. R. Siegfried, Interannual variations in meltwater input to the Southern Ocean from Antarctic ice shelves. *Nat. Geosci.* **13**, 616–620 (2020).
9. H. D. Pritchard, S. R. M. Ligtenberg, H. A. Fricker, D. Vaughan, M. R. Van den Broeke, L. Padman, Antarctic ice-sheet loss driven by basal melting of ice shelves. *Nature* **484**, 502–505 (2012).
10. S. S. Jacobs, A. Jenkins, C. F. Giulivi, P. Dutrieux, Stronger ocean circulation and increased melting under Pine Island Glacier ice shelf. *Nat. Geosci.* **4**, 519–523 (2011).
11. P. Dutrieux, J. De Rydt, A. Jenkins, P. R. Holland, H. K. Ha, S. H. Lee, E. J. Steig, Q. Ding, E. P. Abrahamsen, M. Schröder, Strong sensitivity of Pine Island ice-shelf melting to climatic variability. *Science* **343**, 174–178 (2014).
12. A. Jenkins, D. Shoosmith, P. Dutrieux, S. Jacobs, T. W. Kim, S. H. Lee, H. K. Ha, S. Stammerjohn, West Antarctic ice sheet retreat in the Amundsen Sea driven by decadal oceanic variability. *Nat. Geosci.* **11**, 733–738 (2018).
13. P. R. Holland, T. J. Bracegirdle, P. Dutrieux, A. Jenkins, E. J. Steig, West Antarctic ice loss influenced by internal climate variability and anthropogenic forcing. *Nat. Geosci.* **12**, 718–724 (2019).
14. F. S. Paolo, L. Padman, H. A. Fricker, S. Adusumilli, S. Howard, M. R. Siegfried, Response of Pacific-sector Antarctic ice shelves to the El Niño/Southern Oscillation. *Nat. Geosci.* **11**, 121–126 (2018).
15. M. P. Schodlok, D. Menemenlis, E. Rignot, M. Studinger, Sensitivity of the ice-shelf/ocean system to the sub-ice-shelf cavity shape measured by NASA IceBridge in Pine Island Glacier, West Antarctica. *Ann. Glaciol.* **53**, 156–162 (2012).
16. T.-W. Kim, H. W. Yang, P. Dutrieux, A. K. Wåhlin, A. Jenkins, Y. G. Kim, H. K. Ha, C.-S. Kim, K.-H. Cho, T. Park, J. Park, S. H. Lee, Y.-K. Cho, Interannual variation of modified circumpolar deep water in the Dotson-Getz Trough, West Antarctica. *J. Geophys. Res.* **126**, e2021JC017491 (2021).
17. B. G. M. Webber, K. J. Heywood, D. P. Stevens, K. M. Assmann, The impact of overturning and horizontal circulation in pine island trough on ice shelf melt in the Eastern Amundsen Sea. *J. Phys. Oceanogr.* **49**, 63–83 (2019).
18. T. S. Dotto, A. C. Naveira Garabato, S. Bacon, P. R. Holland, S. Kimura, Y. L. Firing, M. Tsamados, A. K. Wåhlin, A. Jenkins, Wind-driven processes controlling oceanic heat delivery to the Amundsen Sea, Antarctica. *J. Phys. Oceanogr.* **49**, 2829–2849 (2019).
19. B. G. M. Webber, K. J. Heywood, D. P. Stevens, P. Dutrieux, E. P. Abrahamsen, A. Jenkins, S. S. Jacobs, H. K. Ha, S. H. Lee, T. W. Kim, Mechanisms driving variability in the ocean forcing of Pine Island Glacier. *Nat. Comm.* **8**, 14507 (2017).
20. A. Silvano, S. R. Rintoul, B. Peña-Molino, W. R. Hobbs, E. van Wijk, S. Aoki, T. Tamura, G. D. Williams, Freshening by glacial meltwater enhances melting of ice shelves and reduces formation of Antarctic bottom water. *Sci. Adv.* **4**, eaap9467 (2018).
21. A. K. Wåhlin, N. Steiger, E. Darelius, K. M. Assmann, M. S. Glessmer, H. K. Ha, L. Herraiz-Borreguero, C. Heuzé, A. Jenkins, T. W. Kim, A. K. Mazur, J. Sommeria, S. Viboud, Ice front blocking of ocean heat transport to an Antarctic ice shelf. *Nature* **578**, 568–571 (2020).
22. P. Spence, R. M. Holmes, A. M. Hogg, S. M. Griffies, K. D. Stewart, M. H. England, Localized rapid warming of West Antarctic subsurface waters by remote winds. *Nat. Clim. Change* **7**, 595–603 (2017).
23. Y. Nakayama, R. Timmermann, H. H. Hellmer, Impact of West Antarctic ice shelf melting on Southern Ocean hydrography. *The Cryosphere* **14**, 2205–2216 (2020).
24. H. U. Sverdrup, The currents off the coast of Queen Maud Land. *Norsk Geografisk Tidsskrift-Norwegian J. Geogr.* **14**, 239–249 (1953).
25. R. Schubert, A. F. Thompson, K. Speer, L. S. Chretie, Y. Bebieva, The Antarctic Coastal Current in the Bellingshausen Sea. *The Cryosphere* **15**, 4179–4199 (2021).
26. C. Moffat, R. C. Beardsley, B. Owens, N. van Lipzig, A first description of the Antarctic Peninsula Coastal Current. *Deep-Sea Res. II: Top. Stud. Oceanogr.* **55**, 277–293 (2008).
27. P. R. Holland, D. Jenkins, D. M. Holland, Ice and ocean processes in the Bellingshausen Sea, Antarctica. *J. Geophys. Res.* **115**, C05020 (2010).
28. M. P. Schodlok, D. Menemenlis, E. J. Rignot, Ice shelf basal melt rates around Antarctica from simulations and observations. *J. Geophys. Res.* **121**, 1085–1109 (2016).
29. A. M. Thurnherr, S. S. Jacobs, P. Dutrieux, C. F. Giulivi, Export and circulation of ice cavity water in Pine Island Bay, West Antarctica. *J. Geophys. Res. Oceans* **119**, 1754–1764 (2014).
30. D. A. Smith, E. E. Hofmann, J. M. Klinck, C. M. Lascara, Hydrography and circulation of the West Antarctic Peninsula continental shelf. *Deep-Sea Res. I: Oceanogr. Res. Pap.* **46**, 925–949 (1999).
31. R. Bintanja, G. J. van Oldenborgh, S. S. Drijfhout, B. Wouters, C. A. Katsman, Important role for ocean warming and increased ice-shelf melt in Antarctic sea-ice expansion. *Nat. Geosci.* **6**, 376–379 (2013).
32. N. C. Swart, J. C. Fyfe, The influence of recent Antarctic ice sheet retreat on simulated sea ice area trends. *Geophys. Res. Lett.* **40**, 4328–4332 (2013).
33. A. G. Pauling, C. M. Bitz, I. J. Smith, P. J. Langhorne, The response of the Southern Ocean and Antarctic sea ice to freshwater from ice shelves in an Earth system model. *J. Climate* **29**, 1655–1672 (2016).
34. D. T. Bett, P. R. Holland, A. C. Naveira Garabato, A. Jenkins, P. Dutrieux, S. Kimura, A. Fleming, The impact of the Amundsen Sea freshwater balance on ocean melting of the West Antarctic ice sheet. *J. Geophys. Res. Oceans* **125**, e2020JC016305 (2020).
35. M. S. Dinniman, J. M. Klinck, E. E. Hofmann, Sensitivity of circumpolar deep water transport and ice shelf basal melt along the West Antarctic Peninsula to changes in the winds. *J. Climate* **25**, 4799–4816 (2012).
36. S. S. Jacobs, C. F. Giulivi, Large multidecadal salinity trends near the pacific–Antarctic continental margin. *J. Climate* **23**, 4508–4524 (2010).
37. M. Losch, D. Menemenlis, J.-M. Campin, P. Heimbach, C. Hill, On the formulation of sea-ice models. Part 1: Effects of different solver implementations and parameterizations. *Ocean Model.* **33**, 129–144 (2010).
38. H. H. Hellmer, D. J. Olbers, A two-dimensional model for the thermohaline circulation under an ice shelf. *Antarct. Sci.* **1**, 325–336 (1989).
39. A. Jenkins, H. H. Hellmer, D. M. Holland, The role of meltwater advection in the formulation of conservative boundary conditions at an ice–ocean interface. *J. Phys. Oceanogr.* **31**, 285–296 (2001).
40. M. Losch, Modeling ice shelf cavities in a z-coordinate ocean general circulation model. *J. Geophys. Res. Oceans* **113**, C08043 (2008).
41. D. M. Holland, A. Jenkins, Modeling thermodynamic ice–ocean interactions at the base of an ice shelf. *J. Phys. Oceanogr.* **29**, 1787–1800 (1999).
42. G. Forget, J.-M. Campin, P. Heimbach, C. N. Hill, R. M. Ponte, C. Wunsch, ECCO version 4: An integrated framework for non-linear inverse modeling and global ocean state estimation. *Geosci. Model Dev.* **8**, 3071–3104 (2015).
43. V. Daru, C. Tenaud, High order one-step monotonicity-preserving schemes for unsteady compressible flow calculations. *J. Comput. Phys.* **193**, 563–594 (2004).
44. B. Fox-Kemper, D. Menemenlis, Can large eddy simulation techniques improve mesoscale rich ocean models?, in *Ocean Modeling in an Eddying Regime*, M. Hecht and H. Hasumi, Eds. (American Geophysical Union, 2008), pp. 319–338.

45. W. G. Large, J. C. McWilliams, S. C. Doney, Oceanic vertical mixing: A review and a model with a nonlocal boundary layer parameterization. *Rev. Geophys.* **32**, 363–403 (1994).

46. A. Adcroft, C. Hill, J. A. Marshall, Representation of topography by shaved cells in a height coordinate ocean model. *Mon. Weather Rev.* **125**, 2293–2315 (1997).

47. J. E. Arndt, H. W. Schenke, M. Jakobsson, F. O. Nitsche, G. Buys, B. Goleby, M. Rebesco, F. Bohoyo, J. Hong, J. Black, R. Greku, G. Udintsev, F. Barrios, W. Reynoso-Peralta, M. Taisei, R. Wigley, The International Bathymetric Chart of the Southern Ocean (IBCSO) Version 1.0—a new bathymetric compilation covering circum-Antarctic waters. *Geophys. Res. Lett.* **40**, 3111–3117 (2013).

48. M. Morlighem, E. Rignot, T. Binder, D. D. Blankenship, R. Drews, G. Eagles, O. Eisen, F. Ferraccioli, R. Forsberg, P. Fretwell, V. Goel, J. S. Greenbaum, H. Gudmundsson, J. Guo, V. Helm, C. Hofstede, I. Howat, A. Humbert, W. Jokat, N. B. Karlsson, W. Lee, K. Matsuoka, R. Millan, J. Mouginot, J. Paden, F. Pattyn, J. L. Roberts, S. Rosier, A. Ruppel, H. Seroussi, E. C. Smith, D. Steinhage, B. Sun, M. R. van den Broeke, T. van Ommen, M. van Wessem, D. A. Young, Deep glacial troughs and stabilizing ridges unveiled beneath the margins of the Antarctic ice sheet. *Nat. Geosci.* **13**, 132–137 (2020).

49. Y. Nakayama, D. Menemenlis, M. Schodlok, E. Rignot, Amundsen and Bellingshausen Seas simulation with optimized ocean, sea ice, and thermodynamic ice shelf model parameters. *J. Geophys. Res.* **122**, 6180–6195 (2017).

50. E. Rignot, S. Jacobs, J. Mouginot, B. Scheuchl, Ice-shelf melting around Antarctica. *Science* **341**, 266–270 (2013).

51. H. Hersbach, B. Bell, P. Berrisford, S. Hirahara, A. Horányi, J. Muñoz-Sabater, J. Nicolas, C. Peubey, R. Radu, D. Schepers, A. Simmons, C. Soci, S. Abdalla, X. Abellan, G. Balsamo, P. Bechtold, G. Biavati, J. Bidlot, M. Bonavita, G. D. Chiara, P. Dahlgren, D. Dee, M. Diamantakis, R. Dragani, J. Flemming, R. Forbes, M. Fuentes, A. Geer, L. Haimberger, S. Healy, R. J. Hogan, E. Holm, M. Janisková, S. Keeley, P. Laloyaux, P. Lopez, C. Lupu, G. Radnoti, P. de Rosnay, I. Rozum, F. Vamborg, S. Villaume, J.-N. Thépaut, The ERA5 global reanalysis. *Q. J. Roy. Meteorol. Soc.* **146**, 1999–2049 (2020).

52. A. S. Gardner, G. Moholdt, T. Scambos, M. Fahnstock, S. Ligtenberg, M. van den Broeke, J. Nilsson, Increased West Antarctic and unchanged East Antarctic ice discharge over the last 7 years. *The Cryosphere* **12**, 521–547 (2018).

53. F. Roquet, C. Wunsch, G. Forget, P. Heimbach, C. Guinet, G. Reverdin, J. Charrassin, F. Bailleul, D. P. Costa, L. A. Huckstadt, K. T. Goetz, K. M. Kovacs, C. Lydersen, M. Biuw, O. A. Nøst, H. Bornemann, J. Ploetz, M. N. Bester, T. McIntyre, M. C. Muelbert, M. A. Hindell, C. R. McMahon, G. Williams, R. Harcourt, I. C. Field, L. Chafik, K. W. Nicholls, L. Boehme, M. A. Fedak, Estimates of the Southern Ocean general circulation improved by animal-borne instruments. *Geophys. Res. Lett.* **40**, 6176–6180 (2013).

54. F. Roquet, J.-B. Charrassin, S. Marchand, L. Boehme, M. Fedak, G. Reverdin, C. Guinet, Delayed-mode calibration of hydrographic data obtained from animal-borne satellite relay data loggers. *J. Atmos. Oceanic Tech.* **28**, 787–801 (2011).

55. X. Zhang, A. F. Thompson, M. M. Flexas, F. Roquet, H. Bornemann, Circulation and meltwater distribution in the Bellingshausen Sea: From shelf break to coast. *Geophys. Res. Lett.* **43**, 6402–6409 (2016).

56. L. M. Schulze Chretien, A. F. Thompson, M. M. Flexas, K. Speer, N. Swaim, R. Oelerich, X. Ruan, R. Schubert, C. LoBuglio, The shelf circulation of the Bellingshausen Sea. *J. Geophys. Res. Oceans* **126**, e2020JC016871 (2021).

57. D. P. Walker, A. Jenkins, K. M. Assmann, D. R. Shoosmith, M. A. Brandon, Oceanographic observations at the shelf break of the Amundsen Sea, Antarctica. *J. Geophys. Res. Oceans* **118**, 2906–2918 (2013).

58. C. Moffat, M. Meredith, Shelf–ocean exchange and hydrography west of the Antarctic Peninsula: A review. *Phil. Trans. Roy. Soc. A* **376**, (2018).

59. Y. Nakayama, R. Timmermann, C. B. Rodehacke, M. Schröde, H. H. Hellmer, Modeling the spreading of glacial meltwater from the Amundsen and Bellingshausen Seas. *Geophys. Res. Lett.* **41**, 7942–7949 (2014).

60. L. C. Biddle, K. J. Heywood, J. Kaiser, A. Jenkins, Glacial meltwater identification in the Amundsen Sea. *J. Phys. Oceanogr.* **47**, 933–954 (2017).

61. A. Beckmann, R. Timmermann, Circumpolar influences on the Weddell Sea: Indication of an Antarctic circumpolar coastal wave. *J. Climate* **14**, 3785–3792 (2001).

62. G. Danabasoglu, J. Lamarque, J. Bacmeister, D. A. Bailey, A. K. DuVivier, J. Edwards, L. K. Emmons, J. Fasullo, R. Garcia, A. Gettelman, C. Hannay, M. M. Holland, W. G. Large, P. H. Lauritzen, D. M. Lawrence, J. T. M. Lenaerts, K. Lindsay, W. H. Lipscomb, M. J. Mills, R. Neale, K. W. Oleson, B. Otto-Bliesner, A. S. Phillips, W. Sacks, S. Tilmes, L. van Kampenhout, M. Vertenstein, A. Bertini, J. Dennis, C. Deser, C. Fischer, B. Fox-Kemper, J. E. Kay, D. Kinnison, P. J. Kushner, V. E. Larson, M. C. Long, S. Mickelson, J. K. Moore, E. Nienhouse, L. Polvani, P. J. Rasch, W. G. Strand, The Community Earth System Model Version 2 (CESM2). *J. Adv. Model. Earth Syst.* **12**, 2019MS001916 (2020).

63. V. Eyring, S. Bony, G. A. Meehl, C. A. Senior, B. Stevens, R. J. Stouffer, K. E. Taylor, Overview of the Coupled Model Intercomparison Project Phase 6 (CMIP6) experimental design and organization. *Geosci. Model Dev.* **9**, 1937–1958 (2016).